# Effects of doping substitutions on the thermal conductivity of half-Heusler compounds

Mauro Fava,[1,*,†] Bonny Dongre,[2,*] Jesús Carrete,[2] Ambroise van Roekeghem,[1] Georg K. H. Madsen,[2] and Natalio Mingo[1]

[1]*Université Grenoble Alpes, CEA, LITEN, 17 rue des Martyrs, 38054 Grenoble, France*

[2]*Institute of Materials Chemistry, TU Wien, Vienna A-1060, Austria*

(Received 11 March 2021; accepted 6 May 2021; published 20 May 2021)

The promise posed by half-Heusler compounds as thermoelectric materials depends on their thermal conductivity, which is strongly affected by doping. Here we elucidate the effect of $p$ dopants on the lattice thermal conductivity ($\kappa_{ph}$) of seven selected half-Heusler compounds and for twelve different substitutional defects. We unveil a strong reduction in $\kappa_{ph}$ even for low concentrations of transition-metal substitutional atoms. Furthermore, we quantify the strength of the bond perturbation induced by substitutional impurities and interpret it in terms of the changes in the local electronic density of states. In several cases we find a significant destructive interference between the mass difference and bond perturbations which reduces the phonon scattering rates below the value expected if the two effects were treated independently. We compare our first-principles calculations with the available experimental measurements on the thermal conductivity of $(Zr, Hf)_{Nb}$-doped NbFeSb and $Sn_{Sb}$-doped ZrCoSb. For the latter, including the effect of independent Co vacancies and interstitials yields an almost perfect agreement with experiment.

DOI: 10.1103/PhysRevB.103.174112

## I. INTRODUCTION

Thermoelectric materials are defined by the fact that they develop an electric potential difference when subject to a thermal gradient. A closed circuit comprising two thermoelectric materials with different Seebeck coefficients can generate an electric current under a temperature difference between the two junctions of the materials [1]. The efficiency of this conversion from thermal to electrical energy is directly related to the value of the materials' thermoelectric figures of merit [2]. For a single material, it is defined as

$$zT = \frac{S^2\sigma T}{\kappa}, \tag{1}$$

where $S$ is the Seebeck coefficient, $\sigma$ is the electrical conductivity, and $\kappa = \kappa_{el} + \kappa_{ph}$ is the thermal conductivity, split into its electronic and phononic contributions.

Several previous experimental [3,4] and theoretical publications on half-Heusler compounds have mainly focused on the electronic contributions to the $zT$ expression, with a particular interest in the power factor $S^2\sigma$, the analysis of the correlation between bonding properties and carrier mobility [5], and the treatment of the electronic relaxation times [6], which requires going beyond the constant relaxation time approximation (RTA) often employed in the case of simple metals. To extract $\kappa_{el}$ the Wiedemann-Franz law is usually employed. Since a low thermal conductivity is required to optimize $zT$, it is of paramount importance to be able to reduce $\kappa_{ph}$ as well as maximize the electronic power factor $\sigma S^2$. This optimization can be achieved by nanostructuring and/or doping.

Past works on doped and alloyed half-Heusler compounds, including Refs. [3,4], used simplified phonon-defect scattering models for the computation of $\kappa_{ph}$. Several of these works considered only the mass difference between host and substituted atom [7] as the source of phonon scattering, while others included the defect-induced change in the local chemistry at the empirical model level [8–10], or did not consider at all the role played by impurities [5]. Therefore, a first-principles understanding of how dopants affect $\kappa_{ph}$ in these materials, considering the perturbation induced by changes in bonds and force constants, is still lacking.

A first step to optimize thermoelectric properties is to identify the most suitable materials. A recent high-throughput study [11] identified a set of $p$-type half-Heusler compounds that optimize the thermoelectric figure of merit while retaining a relatively high abundance of constituent elements, namely VFeSb, TaFeSb, NbFeSb, NbCoSn, TaCoSn, ZrCoSb, and HfCoSb. In that study, a set of stable substitutional impurities was found, specifically $(Ti, Hf)_V$ (VFeSb), $(Ti, Hf, Zr)_{Nb}$ (NbFeSb and NbCoSn), $(Ti, Hf, Zr)_{Ta}$ (TaFeSb), $Hf_{Ta}$ in TaCoSn, $Sc_{Zr}$(Hf) [Zr(Hf)CoSb], $Mn_{Fe}$ (NbFeSb and TaFeSb), and $Sn_{Sb}$ (NbFeSb, TaFeSb, ZrCoSb, and HfCoSb). Here we use theoretical methods to study the effect of this set of defects in their charged states on the thermal conductivity of the aforementioned materials. Although it is often assumed that the amount of $\kappa_{ph}$ reduction is correlated with the normalized mass difference between host and defect atoms, we show that this is not generally true when the substituted atom is a transition metal. Instead, we identify a strong effect due to the local bond perturbation induced by dopants. This effect must be taken into account in order to get an accurate description

*These authors contributed equally to this work.
†Mauro.FAVA@cea.fr

 ©2021 American Physical Society

of phonon thermal transport as a function of the impurity concentration. We explain how bonds are affected by impurities in terms of the electronic structure of the pristine compounds. We also present an empirical model of the lattice thermal conductivity as a function of temperature and concentration for the considered set of defects and containing the overall effects of change of mass and bonds. Finally, comparison with available measurements suggests that electron-phonon and phonon-boundary scattering are likely to play a measurable role in explaining the lowering of the (Ti,Hf)-doped lattice thermal conductivity of NbFeSb. Instead, in the case of $Sn_{Sb}$-doped ZrCoSb we find that the inclusion of cobalt vacancies and interstitials is of paramount importance to obtain a good agreement with the experimental measurements, in agreement with past works. We further argue that uncorrelated Co vacancies and interstitials are energetically more favorable than Co Frenkel pairs, and show that they are likely the main cause of the low $\kappa$ of tin-doped ZrCoSb.

## II. THEORY

The phonon Boltzmann equation in stationary conditions balances the contributions from drift motion and scattering processes [12,13]. We assume the deviation from equilibrium of the mode populations to be linear under a thermal gradient. Therefore the lattice contribution to the thermal conductivity in a crystal with cubic symmetry reads

$$\kappa_{\rm ph} = \frac{k_B}{\Omega_s}\sum_{\lambda}\left(\frac{\hbar\omega_\lambda}{k_B T}\right)^2 n_\lambda^0\left(n_\lambda^0+1\right)v_\lambda F_\lambda, \tag{2}$$

where $\lambda$ represents the wave vector and branch $(\vec{q}, b)$, $\omega_\lambda$ and $v_\lambda$ are the phonon frequency and group velocity, respectively, and $n_\lambda^0$ is the equilibrium Bose-Einstein distribution. The quantity $F_\lambda \equiv \tau_\lambda(v_\lambda + \Delta_\lambda[F_\lambda])$ represents an effective mean-free path that includes a coupling between phonon states [14], with $\tau_\lambda$ being the phonon relaxation time and $\Delta_\lambda$ a function of $F_\lambda$ itself. In cases where umklapp scattering processes dominate, we can neglect the coupling between modes and work under the single-mode relaxation time approximation (SMRTA) by taking $\Delta_\lambda \equiv 0$.

The relaxation time of a phonon mode can be computed as the inverse of its total scattering rate, which in turn can be computed by applying Matthiessen's rule to the main scattering processes. Here we consider anharmonic three-phonon and two-phonon interactions, where the latter comprise both the contribution from isotopes of the elements of the pristine compounds and from substitutional impurities. Therefore we have

$$\frac{1}{\tau_\lambda} = \frac{1}{\tau_\lambda^{\rm 3ph}} + \frac{1}{\tau_\lambda^{\rm iso}} + \frac{1}{\tau_\lambda^{\rm def}}. \tag{3}$$

The anharmonic three-phonon scattering rates can be evaluated from first principles by computing the third-order force constants [15,16], while to assess the phonon-isotope interaction we can apply the expression derived by Tamura [17,18]. Lowest-order perturbation theory is often accurate enough to evaluate anharmonic and isotope scattering, but the Fermi golden rule has often proven to be unreliable at dealing with external defects [19]. Thus a $T$-matrix supercell-based approach has been developed [20,21] to treat the substitutional impurities that involve both a mass $V_M$ and a bond perturbation $V_K$ near the impurity. The total perturbation is defined as $V = V_M + V_K$, with

$$V_M^{ij,\alpha\beta}(\omega_\lambda) = -\omega_\lambda^2\frac{\tilde{M}_i - M_j}{M_i}\delta_{ij}\delta_{\alpha\beta} \tag{4}$$

and

$$V_K^{ij,\alpha\beta} = \frac{\tilde{K}^{ij,\alpha\beta} - K^{ij,\alpha\beta}}{\sqrt{M_i M_j}}, \tag{5}$$

where $\alpha$, $\beta$ and $i$, $j$ are the Cartesian direction and atom labels in the supercell; $M_i$ ($\tilde{M}_i$) is the mass of the host (substitutional) atom at site $i$, and $K^{ij,\alpha\beta}$ ($\tilde{K}^{ij,\alpha\beta}$) is the harmonic force constant tensor element between atoms $i$ and $j$ in the pristine (defect-laden) supercell. As the bond perturbation can be assumed to be short ranged and it is evaluated in real space, we can define the cutoffs $r_{\rm cut}$ and $R_{\rm cut}$ to reduce the computational burden of its evaluation. Here $r_{\rm cut}$ represents the maximum interaction distance between a pair of atoms, where both of them belong to the sphere defined by $R_{\rm cut}$ and centered at the defect site. After specifying the cutoffs, the acoustic sum rule for $V_K$ is enforced by projecting away the degrees of freedom that correspond to rigid translations according to the procedure developed in Ref. [22]. The pristine retarded Green's function can be computed in real space for the atoms specified by the cutoffs:

$$\langle i\alpha|\, g^+(\omega^2)\,|j\beta\rangle = \sum_\lambda \langle i\alpha|\,\lambda\rangle\langle\lambda\,|j\beta\rangle\left(\omega^2 - \omega_\lambda^2 + i0^+\right)^{-1}, \tag{6}$$

and once $V$ is known, the scattering matrix $T$ can be evaluated to all orders as

$$T^+[V] = (1 - Vg^+)^{-1}V. \tag{7}$$

Since we are interested in the dilute limit, we use a single-defect approximation, with the $V$ perturbation containing the contribution from a single impurity embedded in the system rather than a distribution. We calculate the scattering rates using the optical theorem:

$$\frac{1}{\tau_\lambda^{\rm ph\text{-}def}} = -\chi\frac{V_{\rm uc}}{\omega_\lambda}{\rm Im}\,\langle\lambda|\,T^+[V]\,|\lambda\rangle\,, \tag{8}$$

where $\chi$ is the volume concentration of impurities in the system and $V_{\rm uc}$ is the unit cell volume. It is worth noting that $T^+[V] \neq T^+[V_M] + T^+[V_K]$. Namely, Matthiessen's rule does not apply to the mass and force constant perturbations induced by the defects. To assess the deviation of the true scattering rates, Eq. (8), from a Matthiessen-like formulation, we compute

$$\left(\frac{1}{\tau_\lambda^{\rm ph\text{-}def}}\right)_{V_M} = -\chi\frac{V_{\rm uc}}{\omega_\lambda}{\rm Im}\,\langle\lambda|\,T^+[V_M]\,|\lambda\rangle\,, \tag{9}$$

$$\left(\frac{1}{\tau_\lambda^{\rm ph\text{-}def}}\right)_{V_K} = -\chi\frac{V_{\rm uc}}{\omega_\lambda}{\rm Im}\,\langle\lambda|\,T^+[V_K]\,|\lambda\rangle\,, \tag{10}$$

and $\tilde{\tau}^{-1}_{\lambda;\rm ph\text{-}def} \equiv \tau^{-1}_{\lambda;\rm ph\text{-}def}[V_M] + \tau^{-1}_{\lambda;\rm ph\text{-}def}[V_K]$. Since at the second order the $T$ matrix can be written as $V + Vg^+V$ and $\tau^{-1}_{\lambda;\rm ph\text{-}def}$ as $-\chi V_{uc}\sum_{\lambda'}|\,\langle\lambda|\,V\,|\lambda'\rangle\,|^2\delta(\omega_\lambda^2 - \omega_{\lambda'}^2)$, this prompts

us to identify the deviations from Matthiessen's rule as due to interference effects between mass and bond induced perturbations.

#### Numerical approach

The phonon calculations have been performed with the VASP [23–25] DFT code using the plane-augmented wave (PAW) [26,27] formalism under the generalized gradient approximation (GGA) in the PBE [28,29] parametrization. VASP calculations were performed in a $4 \times 4 \times 4$ supercell at the Gamma point, with plane-wave cutoffs set up according to the "Accurate" precision tag and all other settings being similar to Ref. [11]. Details on the structural relaxation can be found there. We have computed the second-order force constants (IFC2) for all pristine and defect-laden systems in the case of a relaxed $4 \times 4 \times 4$ (192-atom) supercell using the small-displacement method. The supercells and the atomic displacements are created with the help of the code Phonopy [30,31], which is also employed to evaluate the force constants following DFT calculations. To calculate $V_K$, we first proceeded by taking the difference between the IFC2s of the pristine and the defect-laden system. We have selected the cutoffs $r_{\text{cut}}$ and $R_{\text{cut}}$ to be 0.6–0.8 nm for all the considered dopants after convergence tests. The scattering $T$ matrix is then calculated using $V = V_K + V_M$ and the pristine retarded Green's function is evaluated using the analytical tetrahedron method and a $16 \times 16 \times 16$ grid. To calculate the three-phonon scattering rates, we use the "thirdorder_vasp.py" code [32] in conjunction with VASP and almaBTE [33]. The phonon-substitution defect scattering rates are combined with the three-phonon and phonon-isotope scattering rates at the relaxation time approximation level using Matthiessen's rule inside the almaBTE code. We used a converged $28 \times 28 \times 28$ transport wave vector mesh to solve the phonon BTE. The validity of the SMRTA in the case of the pristine systems was tested by solving Eq. (2) also in the $\Delta_\lambda \neq 0$ case. A good agreement between the relaxation time approximation and the full self-consistent solution was found for all the considered pristine materials, with $|\kappa_{\text{ph}}^{SMRTA} - \kappa_{\text{ph}}^{\text{iter}}|/\kappa_{\text{ph}}^{\text{iter}} \leqslant 6\%$ in the considered 300–400 K temperature range.

## III. RESULTS

### A. Classification of the compounds and the considered substitutions

Half-Heusler compounds typically have either 8 or 18 valence electrons [34–36]. Here we consider compounds with electron count = 18. Possible ways of constructing these compounds are sketched in Fig. 1. The half-Heusler structure comprises three species in the 1:1:1 stoichiometry. The two geometrically equivalent sites are labeled as $A$ and $A'$, and the inequivalent one is labeled as $B$. Following Ref. [11], we consider compounds involving periodic table columns 8 or 9 for the $B$ site, 4 or 5 for the $A$ site, and columns IV or V for the $A'$ site. Species on sites $A$ and $B$ are transition metals, but the one on $A'$ is not. Thus we can define three groups of compounds, in terms of the columns involved: 4-9-V, 5-9-IV, and 5-8-V.

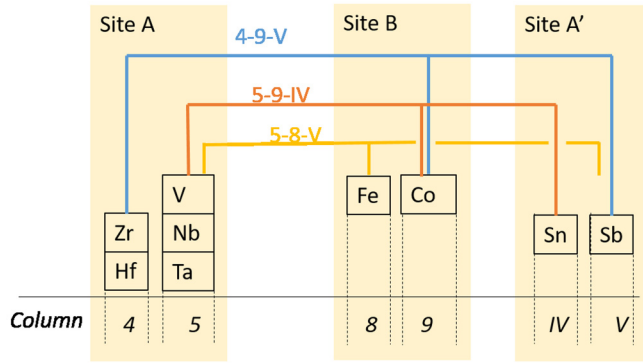


FIG. 1. Ways of combining the species to construct the 18 electron count compounds considered.

For each of these groups, $p$-doping substitutions can in principle be carried out on any of the three sites, replacing a species by another one from the column on its left-hand side. The possibilities that yielded stable substitutions in Ref. [11] are shown in Table I.

### B. A descriptor for phonon-defect scattering

To better assess the magnitude of the scattering rates for each dopant and material we can use a descriptor defined as follows:

$$D_{\text{def};V} \equiv \frac{1}{N} \sum_{\lambda} \tau_{\lambda;V}^{-1}, \tag{11}$$

where $N$ is the number of $\vec{q}$ points in the reciprocal space grid, and $\tau_{\lambda;V}$ is the relaxation time computed with either the bond $V_K$, mass $V_M$, or total $V = V_M + V_K$ perturbation; see Eqs. (8)–(10). This descriptor aims at giving a scalar and temperature-independent representation of the magnitude of the scattering mechanisms for each of the considered dopants and materials. In Table II we show the value of normalized mass variance for each defect and material.

The values of this descriptor in the case of VFeSb are reported in Fig. 2. The mass perturbation from the two considered impurities clearly follows the mass variances trend, with a much stronger contribution from the $\text{Hf}_{\text{V}}^{-1}$ substitution. We note that most of the defect-induced perturbation is attributable to a change in the local bonds in the case of the $\text{Ti}_{\text{V}}^{-1}$ impurity where the mass part of the perturbation is negligibly small. The contribution from $V_K$ is particularly relevant for the $\text{Hf}_{\text{V}}^{-1}$ defect, although in this case the effect coming from the force constant difference is present along

TABLE I. Stable substitution schemes considered.

| Substitution scheme | Cases |
|---|---|
| $\mathbf{3_4}$-9-V | $\mathbf{Sc_{(Zr,Hf)}}$-Co-Sb |
| $\mathbf{4_5}$-{9-IV, 8-V} | $(\mathbf{Ti, Zr, Hf})_{(\mathbf{V,Nb,Ta})}$-{Fe-Sb, Co-Sn} |
| 5-$\mathbf{7_8}$-V | (V, Nb, Ta)-$\mathbf{Mn_{Fe}}$-Sb |
| {4-9, 5-8}-$\mathbf{IV_V}$ | {(Zr, Hf)-Co, (V, Nb, Ta)-Fe}-$\mathbf{Sn_{Sb}}$ |

TABLE II. Absolute mass difference normalized by the host atom mass for each substitution impurity.

| | $Ti_V^{-1}$ | $Ti_{Nb}^{-1}$ | $Ti_{Ta}^{-1}$ | $Hf_V^{-1}$ | $Hf_{Nb}^{-1}$ | $Hf_{Ta}^{-1}$ | $Zr_{Nb}^{-1}$ | $Zr_{Ta}^{-1}$ | $Sc_{Hf}^{-1}$ | $Sc_{Zr}^{-1}$ | $Sn_{Sb}^{-1}$ | $Mn_{Fe}^{-1}$ |
|---|---|---|---|---|---|---|---|---|---|---|---|---|
| $\Delta M/M_0$ | 0.06 | 0.48 | 0.735 | 2.50 | 0.92 | 0.01 | 0.02 | 0.4958 | 0.75 | 0.50 | 0.025 | 0.016 |

with a much larger mass substitution than that for Ti. We also notice that the descriptor for the total perturbation stems from a destructive interference between the mass and bond perturbation contributions for the Hf substitution.

In Figs. 3 and 4 we show the values of the descriptor for the dopants of TaFeSb and NbFeSb, respectively. The mass perturbation is negligibly small in the $Sn_{Sb}^{-1}$, $Mn_{Fe}^{-1}$, and $Hf_{Ta}^{-1}$ ($Zr_{Nb}^{-1}$) cases, following the periodic table. The tin substitution also leads to a small value for the bond descriptor, compared with the other dopants. The phonon-defect interaction is visibly much stronger when the dopants are Ti and Zr or even Hf and Mn. Combined with a large mass perturbation, the strongest scattering comes from $Ti_{Ta}^{-1}$ and $Zr_{Ta}^{-1}$ for TaFeSb and $Hf_{Nb}^{-1}$ and $Ti_{Nb}^{-1}$ for NbFeSb. A similar phenomenon is found in the cases of NbCoSn and TaCoSn dopants in Fig. 5 with the $Hf_{Nb}^{-1}$ confirmed to give the strongest scattering, this also being due to the large associated $V_M$. A surprisingly large bond perturbation in the $Ti_{Nb}^{-1}$ and $Zr_{Nb}^{-1}$ substitution cases is also observed. We would also like to note, in both NbFeSb and NbCoSn, that the mass descriptor for the $Ti_{Nb}$ impurity is larger than for $Hf_{Nb}$, despite Hf being much heavier than Ti. This can be attributed to the larger rates induced by Ti at medium-high frequency; see Figs. 9– 11 in the Supplemental Material [37]. We finally notice that in both TaFeSb, NbFeSb, and NbCoSn a destructive interference between $V_M$ and $V_K$ under Ti doping lowers the total scattering rates with respect to the pure bond part, similarly to what we observed in VFeSb (Hf substitution). If we now evaluate the last compound of each set, i.e., HfCoSb and ZrCoSb (Fig. 6), we find in both cases that doping with Sn produces a rather small scattering, either of mass or bond origin, while the strongest impact is due to Sc substitution, which leads to strong $V_M$ and $V_K$ terms.

Thus, as a general trend, we find that the $Sn_{Sb}^{-1}$ substitution is responsible for a very weak phonon-defect interaction, while stronger effects can be expected for the remaining dopants. In particular, the $Hf_{Nb}^{-1}$ and $Sc_{Hf}^{-1}$ impurities are the

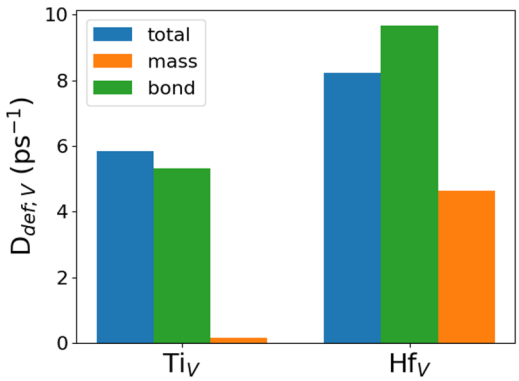


FIG. 2. Phonon-defect scattering rates descriptor for VFeSb dopants. The blue, orange, and green columns indicate respectively the total, mass-only, and bond-only induced-scattering rates.

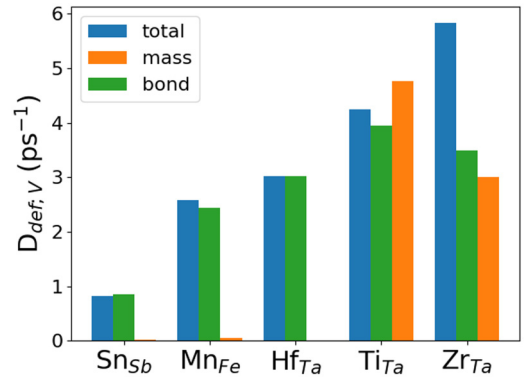


FIG. 3. Phonon-defect scattering rates descriptor for TaFeSb dopants. The blue, orange, and green columns indicate respectively the total, mass-only, and bond-only induced-scattering rates.

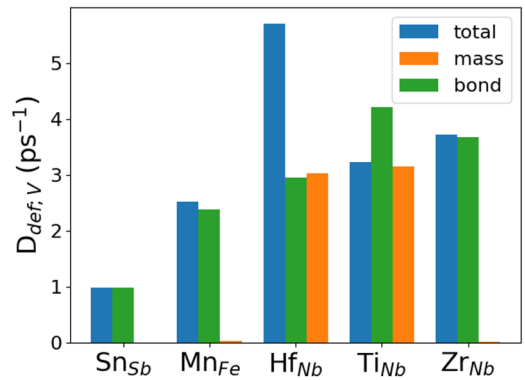


FIG. 4. Phonon-defect scattering rates descriptor for NbFeSb dopants. The blue, orange, and green columns indicate respectively the total, mass-only, and bond-only induced-scattering rates.

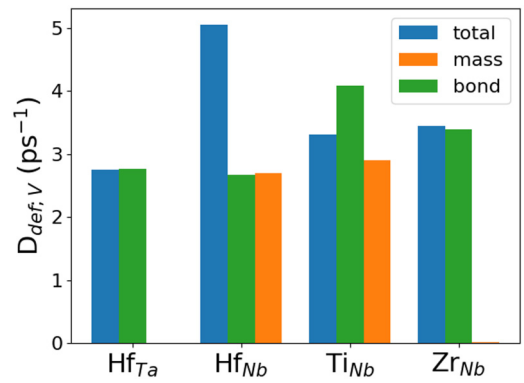


FIG. 5. Phonon-defect scattering rates descriptor for TaCoSn and NbCoSn dopants. The blue, orange, and green columns indicate respectively the total, mass-only, and bond-only induced-scattering rates.

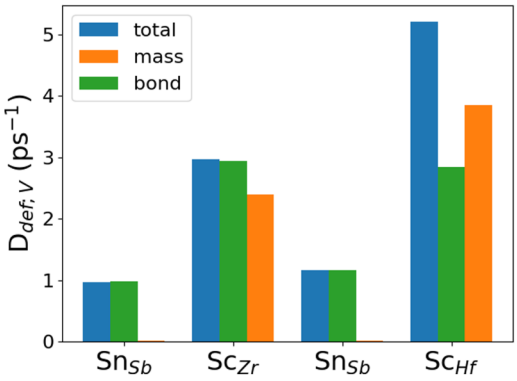


FIG. 6. Phonon-defect scattering rates descriptor for ZrCoSb and HfCoSb dopants. The blue, orange, and green columns indicate respectively the total, mass-only, and bond-only induced-scattering rates.

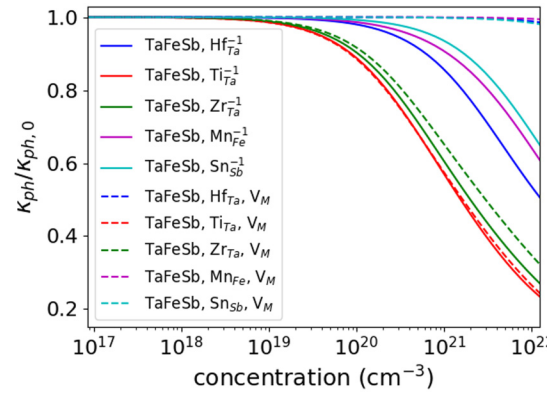


FIG. 8. Thermal conductivity ratio of TaFeSb upon Ti, Hf, Zr, Mn, and Sn doping. Continuous (dashed) lines correspond to total (mass-only) perturbation.

sources for the strongest scattering effects among all the dopants in the set, by virtue of a combined effect of both large mass variance and strong bond perturbation. Of particular interest are the substitutions involving transition metals, specifically in the $Zr_{Nb}^{-1}$, $Hf_{Ta}^{-1}$, and $Ti_{V}^{-1}$ cases. It is common to assume that both mass- and bond-induced perturbations are small for substitutional defects when the impurity and host atoms are adjacent in the periodic table. This is what happens in the Sn substitution case, but not when transition-metal elements are considered, except for Mn.

We can give a simple qualitative explanation for the observed trend in terms of the electronic structure of the parent compounds. Half-Heusler compounds (HHs) have a strong *d*-orbital character near the electronic band gap, as a consequence of containing block-*d* elements [38–41]. On the other hand the *p* contribution to the density of states, coming mostly from elements like Sn and Sb, is much smaller close to the gap. We confirmed this by computing the electronic DOS for all the pristine HHs; see Figs. 1– 7 in the Supplemental Material [37]. Therefore, the substitution of Sb is expected to affect the electronic properties, and thus forces and IFCs, much less than the substitution of a transition-metal element. Unlike the other cases, the $Mn_{Fe}^{-1}$ substitution takes place on the *B* site. Thus one cannot fairly compare its effect with that of the other transition-metal substitutions. The small scattering rates of the $Mn_{Fe}^{-1}$ case may also be partly the result of the small phonon local density of states on the Fe atom in the lower frequency range (see Figs. 8– 14 in the Supplemental Material [37]).

### C. Phonon thermal conductivity

The pristine thermal conductivity $\kappa_{ph,0}$ at 300 K is shown in Table III for the seven half-Heusler compounds. This section presents the dependence of $\kappa_{ph}/\kappa_{ph,0}$ on the impurity concentration at the temperature of 300 K for all the considered materials and defects. In Figs. 7–11 we report the conductivity normalized by its pristine value in the cases of VFeSb, TaFeSb, NbFeSb, TaCoSn, NbCoSn, ZrCoSb, and HfCoSb upon doping. All defects are considered in their charged acceptor state, and dashed lines indicate the use of the mass perturbation only, while solid lines correspond to the total perturbation $V = V_K + V_M$ case. The conductivity curves partly reflect the trend observed for the descriptor. In general we find that Sn and Mn do not affect the thermal conductivity by much, lowering it by only 20% at concentrations $\sim 10^{21}$ cm$^{-3}$. On the other hand, the conductivities of HfCoSb and ZrCoSb

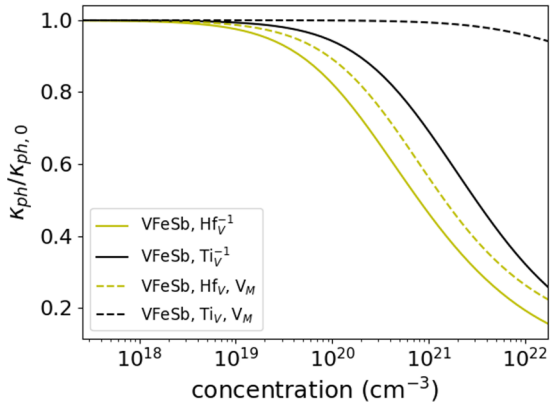


FIG. 7. Thermal conductivity ratio of VFeSb upon Ti and Hf doping. Continuous (dashed) lines correspond to total (mass-only) perturbation.

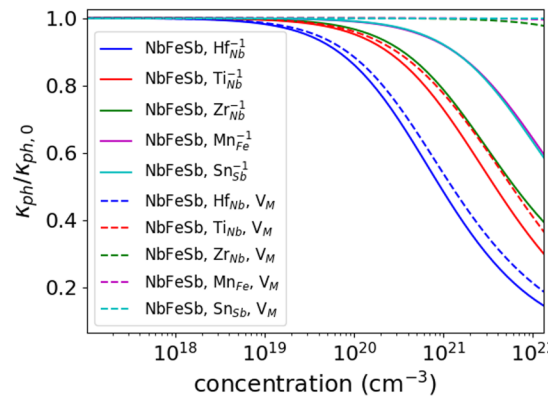


FIG. 9. Thermal conductivity ratio of NbFeSb upon Ti, Hf, Zr, Mn, and Sn doping. Continuous (dashed) lines correspond to total (mass-only) perturbation.

TABLE III. Thermal conductivity of the pristine compounds at 300 K.

| | VFeSb | NbFeSb | NbCoSn | TaFeSb | TaCoSn | HfCoSb | ZrCoSb |
|---|---|---|---|---|---|---|---|
| $\kappa_{\mathrm{ph},0}$ (W K$^{-1}$ m$^{-1}$) | 15.6 | 22.6 | 16.3 | 15.9 | 16.8 | 21.8 | 21.9 |

are reduced by as much as 40%–50% at the same concentration upon Sc doping. A similarly large reduction is observed in the case of NbCoSn when Nb is substituted by Hf or TaFeSb when Ta is substituted by Ti or Zr. The largest reduction at $\chi \sim 10^{21}$ cm$^{-3}$ is observed for VFeSb and NbFeSb when V or Nb are substituted by Hf, where the conductivity presents a decrease of ∼60% of its pristine value. These results can be understood in terms of the large phonon-defect scattering rates shown in Figs. 2 and 4.

The difference between total and mass contribution to the conductivity decrease is feeble when $V_M$ is large. This can be seen in the $\mathrm{Hf_V^{-1}}$, $\mathrm{Ti_{Ta}^{-1}}$, $\mathrm{Zr_{Ta}^{-1}}$, $\mathrm{Hf_{Nb}^{-1}}$, $\mathrm{Ti_{Nb}^{-1}}$, and Sc substitutional cases. On the other hand the effect of $V_K$ is much more noticeable in those transition-metal substitutions where the impurity replaces its adjacent atom in the periodic table, namely $\mathrm{Ti_V^{-1}}$, $\mathrm{Zr_{Nb}^{-1}}$, and $\mathrm{Hf_{Ta}^{-1}}$. The value of $\kappa_{\mathrm{ph}}$ is in general correlated with the normalized mass difference between the impurity and the substituted atom, but some exceptions appear. This happens in the $\mathrm{Ti_V^{-1}}$, $\mathrm{Zr_{Nb}^{-1}}$, and $\mathrm{Hf_{Ta}^{-1}}$ cases, which have a relevant impact on the thermal conductivity of VFeSb, NbFeSb/NbCoSn, and TaFeSb/TaCoSn, respectively, despite presenting a very weak mass perturbation and having similar atomic radii to the atom they substitute. Furthermore, the correlation with $\Delta M/M_0$ does not exclude the possibility of a correlation with the change in the local chemistry represented by $V_K$, which is the case of several V, Nb, Ta, Hf, and Zr substitutionals, as also seen in Figs. 2–6.

### D. Interference effects

We have seen hints of destructive interference between the contributions from $V_M$ and $V_K$ to the scattering rate descriptor in several impurities (see Figs. 20–24 in the Supplemental Material [37]). It is thus instructive to see how the previous thermal conductivity results differ from a model that (incorrectly) applied Matthiessen's rule to the bond-only and mass-only scattering rates. In Fig. 12 we notice that decoupling the mass and bond contributions to the phonon-impurity rates can lower $\kappa_{\mathrm{ph}}$ by a further ∼10% with respect to the correct formulation of $\tau^{-1}_{\lambda,\text{ph-def}}$. The effect of this overestimation is particularly visible when the dopant is Ti.

Furthermore, the descriptor $D$ sometimes predicts that the overall scattering can be weaker than that caused by the bond or the mass perturbation alone. This occurs for $\mathrm{Hf_V}$ in VFeSb, $\mathrm{Ti_{Ta}}$ in TaFeSb, and $\mathrm{Ti_{Nb}}$ in NbFeSb and NbCoSn. Similarly to our previous study of resonant phonon scattering [42], we elucidate the effect by calculating the phonon transmission function using a 1D chain with nearest-neighbor interactions as a model system. We include only one substitutional atom with different mass and spring constants. This simple model shows that modifying the mass of the impurity can in certain cases, and at some frequency ranges, lessen the backscattering (i.e., increase the phonon transmission probability) with respect to the case where the impurity's mass is equal to that for the other atoms. The reason for this effect is that the mass and bond perturbations can affect the same elements of the Hamiltonian. Thus, depending on the relative signs of the two perturbations, some of the total perturbation matrix elements can become larger or smaller, in some cases resulting in a lowering of the overall scattering. Details on the model calculation are included in the Supplemental Material [37].

Given Eqs. (4) and (5), we can expect that equal-sign mass and IFC variations would produce perturbations that partially counteract each other. For real materials, although the $V_K$ is a complicated matrix connecting many different degrees of freedom, one may still expect a correlation between $D_V/(D_{V_K}+D_{V_M})$ and $\Delta K_{0,0}$, the latter being the force constant difference at the defect site, as shown in Fig. 13. In particular, we have found that we can have $D_V > (D_{V_K}+D_{V_M})$ if $\Delta M$ and $\Delta K_{0,0}$ have the same sign. This qualitatively

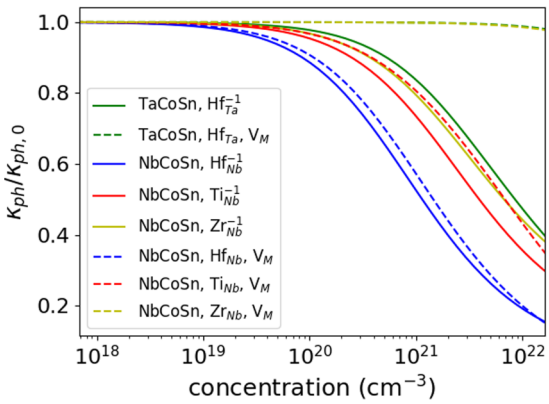


FIG. 10. Thermal conductivity ratio of TaCoSn and NbCoSn upon Hf, Ti, and Zr doping. Continuous (dashed) lines correspond to total (mass-only) perturbation.

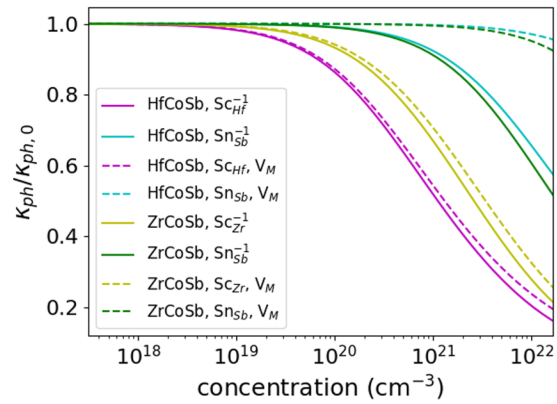


FIG. 11. Thermal conductivity ratio of HfCoSb and ZrCoSb upon Sc and Sn doping. Continuous (dashed) lines correspond to total (mass-only) perturbation.

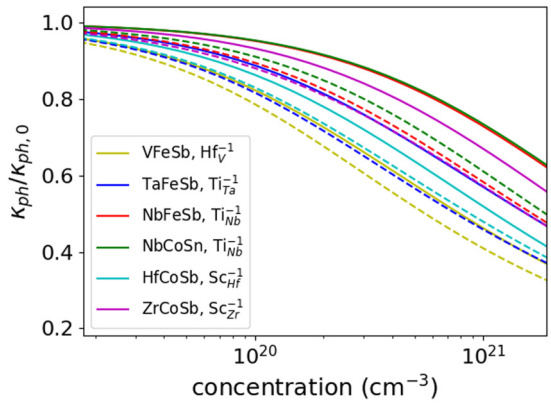


FIG. 12. Thermal conductivity ratio for the "non-Matthiessen" compounds. Continuous lines correspond to phonon-defect scattering rates modeled according to Eq. (8), while dashed lines to Matthiessen's rule applied to $V_M$ and $V_K$.

accounts for the nonadditivity of the scattering matrices for dopants like $Hf_V$ and $Ti_{Ta}$.

### E. Empirical model for $\kappa_{ph}$

It is possible to analytically approximate the thermal conductivity as a function of temperature and doping concentration, including not only the mass perturbation but also the influence of dopants on the local bonds. To do so, we customize an empirical version of the model developed by Klemens [43]. This model assumes a linear phonon dispersion, high temperature limit, and analytical expressions for umklapp and defect induced scattering rates; thus it is unsuitable for a realistic calculation of the conductivity, and it does not include the phonon-defect interaction beyond the Born approximation level. Therefore we define the following empirical equation:

$$\frac{\kappa_{\rm ph}(\chi,T)}{\kappa_{\rm ph,bulk}} = \left(\frac{300\ {\rm K}}{T}\right)\frac{\arctan[\sqrt{f(\chi,T)}]}{\sqrt{f(\chi,T)}} \qquad (12)$$

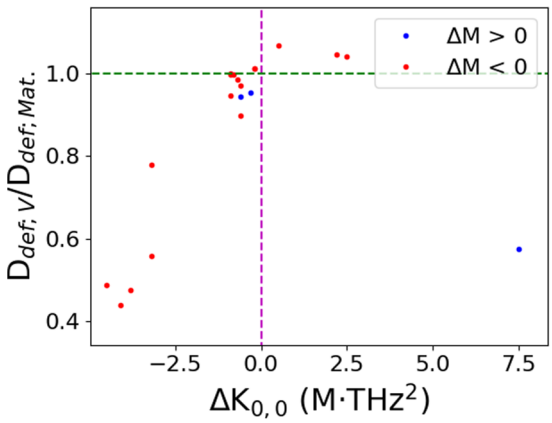


FIG. 13. $D_V/(D_{V_M}+D_{V_K})$ as a function of the defect-site IFC variation $\Delta K_{0,0}$, computed via the DFT+BTE approach.

TABLE IV. Parameters for the empirical model.

| | $\alpha$ | $\beta$ |
|---|---|---|
| VFeSb, $Hf_V^{-1}$ | 116.444 | 0.946 |
| VFeSb, $Ti_V^{-1}$ | 34.749 | 0.975 |
| TaFeSb, $Hf_{Ta}^{-1}$ | 8.0567 | 0.895 |
| TaFeSb, $Ti_{Ta}^{-1}$ | 55.414 | 0.930 |
| TaFeSb, $Zr_{Ta}^{-1}$ | 40.428 | 0.894 |
| TaFeSb, $Mn_{Fe}^{-1}$ | 4.305 | 0.864 |
| TaFeSb, $Sn_{Sb}^{-1}$ | 3.490 | 0.936 |
| NbFeSb, $Hf_{Nb}^{-1}$ | 137.689 | 1.065 |
| NbFeSb, $Ti_{Nb}^{-1}$ | 27.681 | 0.999 |
| NbFeSb, $Zr_{Nb}^{-1}$ | 15.306 | 0.930 |
| NbFeSb, $Mn_{Fe}^{-1}$ | 4.456 | 0.939 |
| NbFeSb, $Sn_{Sb}^{-1}$ | 4.761 | 0.969 |
| TaCoSn, $Hf_{Ta}^{-1}$ | 11.765 | 0.975 |
| NbCoSn, $Hf_{Nb}^{-1}$ | 107.918 | 1.068 |
| NbCoSn, $Ti_{Nb}^{-1}$ | 24.936 | 0.979 |
| NbCoSn, $Zr_{Nb}^{-1}$ | 14.114 | 0.922 |
| HfCoSb, $Sc_{Hf}^{-1}$ | 85.389 | 0.977 |
| HfCoSb, $Sn_{Sb}^{-1}$ | 3.974 | 0.928 |
| ZrCoSb, $Sc_{Zr}^{-1}$ | 40.473 | 1.013 |
| ZrCoSb, $Sn_{Sb}^{-1}$ | 5.321 | 0.978 |

with

$$f(\chi,T) = \alpha\left(\frac{300\ {\rm K}}{T}\right)(\chi V_{uc})^{\beta}. \qquad (13)$$

Table IV lists the parameters $\alpha$ and $\beta$ for each compound and defect. The small nonlinearity with respect to the concentration has been included to better fit the high doping limit, although the $\beta$ exponents are tightly clustered around $\beta_0 \equiv 1$. As this model involves the contribution from both $V_M$ and $V_K$, which has proven to be important for several of the considered impurities, it can be used to estimate the phonon contribution to thermal transport in half-Heusler compounds and properly evaluate the thermoelectric efficiency.

### F. Comparison with experimental data

Figure 14 shows the calculated room temperature $\kappa_{\rm ph}$ for $Nb_{1-x}A_xFeSb$ ($A$ = Ti or Hf) as a function of the concentration of defects—including both the mass and force constant induced perturbations—in comparison with the measurements in Ref. [3]. The lower values of the experimental measurement may come from additional boundary and electron-phonon scattering contributions, not included in the present *ab initio* calculation, as suggested by Refs. [3,7].

In Fig. 15 we further show the thermal conductivity of ZrCoSb as a function of Sn content. The solid lines correspond to the calculated thermal conductivity reduction caused by the $Sn_{Sb}^{-1}$ defect. As expected from the low $D$ value shown in Fig. 6, the $Sn_{Sb}^{-1}$ defects are weak scatterers and result in a relative small suppression of the thermal conductivity on their own.

He *et al.* [44] on the other hand reported a relatively high suppression of the experimental thermal conductivity upon Sn doping of ZrCoSb. These values are shown as squares for two different temperatures in Fig. 15. He *et al.* [44] interpreted

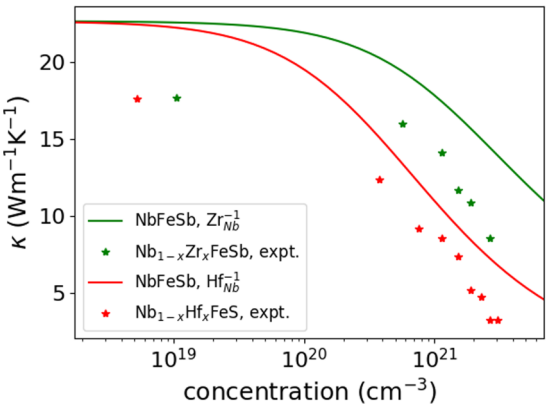


FIG. 14. Thermal conductivity as a function of the concentration for (Zr, Hf)$_{Nb}^{-1}$-doped NbFeSb at 300 K. Continuous line: Total defect perturbation. Stars: Experimental measurements from Ref. [3].

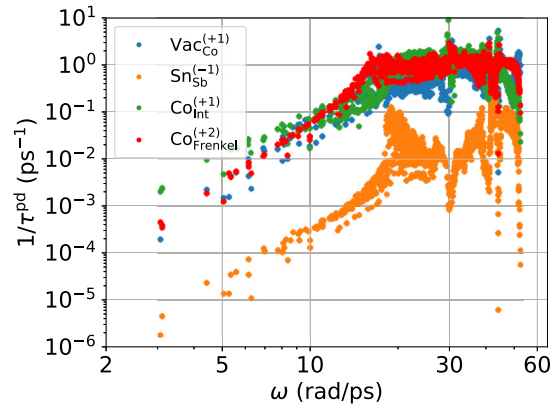


FIG. 16. A comparison of the point-defect phonon scattering rates caused by various defects in ZrCoSb at concentrations of $10^{21}$ cm$^{-3}$.

this as being due to the formation of compensating Frenkel defects. These defects, which can be understood as a Co moving to an neighboring interstitial position and leaving behind a vacancy, act as strong phonon scatterers. This interpretation was corroborated by Rietveld refinement and the relatively low carrier concentration compared to the Sn doping. We have also calculated the scattering rates due to a Frenkel defect, and the resulting scattering rates (red dots in Fig. 16) are almost two orders of magnitude larger than those due to $Sn_{Sb}^{-1}$ defects. Using Frenkel defect concentrations of 1% and 2% as obtained from Rietveld refinement for the $ZrCoSb_{0.8}Sn_{0.2}$ and $ZrCoSb_{0.7}Sn_{0.3}$ samples [44] we get a good agreement with experiment (open circles in Fig. 15). We also point out that if we use a slightly higher Frenkel defect concentration of 2% and 3%, as was done in the empirical model used in Ref. [44], an even better agreement can be obtained.

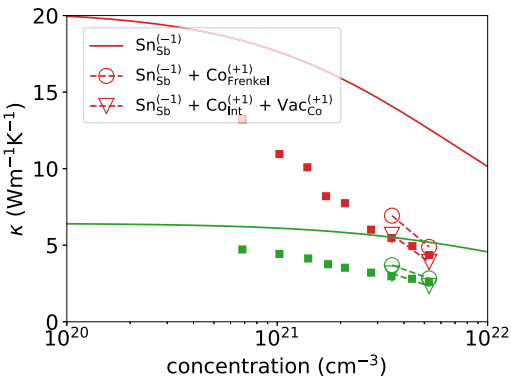


FIG. 15. Thermal conductivity as a function of the Sn concentration for doped ZrCoSb. The squares are the experimental data from Ref. [44]. Red lines and points correspond to 300 K and green to 973 K. The full lines correspond to $\kappa$ calculations when only considering the point-defect phonon scattering caused by the $Sn_{Sb}^{-1}$ defects. The open circles and triangles and dashed lines correspond to the calculated $\kappa$ when considering additional phonon scattering due to the presence of Frenkel defects, and vacancy plus interstitial defects, respectively. Concentrations of 1% and 2% were used corresponding to the Rietveld refinement in Ref. [44].

While our methods allow us to reproduce the conclusions of Ref. [44], we feel that some steps along the chain of arguments are open to a different interpretation. In Fig. 9 of Ref. [44], the $Co_{Frenkel}^{+1}$ defects can be seen to be high in energy at the valence band maximum, with their formation energies being substantially higher than the combined formation energy of isolated $Co_{Int}^{+1}$ and $Vac_{Co}^{+1}$ defects. Entropy maximization would further favor distributing interstitials and vacancies randomly throughout the crystal. The separate formation of interstitials and vacancies is thus thermodynamically favored over Frenkel defects, which can be seen as interstitial-vacancy pairs. Figure 16 shows that the scattering rates of the isolated defects are similar to those of the Frenkel defect. Two isolated defects would thus have approximately double the scattering strength of the combined Frenkel defect. We consequently construct a model where the defect scattering is due to isolated $Sn_{Sb}^{-1}$, $Co_{Int}^{+1}$, and $Vac_{Co}^{+1}$ defects. For simplicity and to stay in line with the Rietveld refinement model in Ref. [44] we use the same interstitial and vacancy concentrations. Now using the concentrations of 1% and 2% obtained via Rietveld refinement and the corresponding 20% and 30% tin content we obtain an almost perfect agreement with experiment. Therefore, we conclude that the experimentally observed $\kappa$ reduction primarily originates from phonon scattering due to isolated defects. In the present case, we see exceptionally high doping leading to the formation of charge-compensating defects which add to scattering, whereas in other systems like Si it leads to significant phonon scattering due to the charge carriers [45]. Furthermore, there is no thermodynamic argument for keeping the interstitial and vacancy concentrations, and the substantial presence of transition-metal interstitials in the full-Heusler position falls in line with the observation of a large phase width in the *n*-type $TiNi_{1+x}Sn$ half-Heusler compound [46,47].

## IV. CONCLUSIONS

We have computed the total scattering rates induced by substitutional impurities, considering the contributions from both the local change of mass $V_M$ and of the bond force constants $V_K$, for a selected group of half-Heusler compounds and their dopants. Aside from the magnitude of $V_M$, which

can be inferred from Table II, the general finding is that the substitutions of transition metals produce a much larger $V_K$ compared with the substitution of non-*d*-block elements, like Sb by Sn. This thus shows that if an element is replaced by an adjacent atom in the periodic table, the change in the local chemistry is not necessarily small. Among the transition-metal substitutions, the one of Mn by Fe yields the smallest scattering rates. This may be attributed to the small vibrational density of states on the Fe atom in the acoustic frequency range of the studied compounds. The scattering probability by Fe substituting impurities is roughly proportional to this density of states, therefore being weak for the acoustic branches.

The strong *d*-orbital character of the considered compounds makes the electronic structure and IFCs much more sensitive to impurities when the substituted atom is the one with the *d* character and/or when the host atom has a large phonon DOS weight. This is arguably the reason for the much smaller scattering rates—and, as consequence, for the much slower decrease of $\kappa_{ph}$ as a function of the defect concentration—that we observe in Sb/Sn substitutions, compared with transition metals. In particular, the dopants that affect $\kappa_{ph}$ the most are Hf (replacing V and Nb in VFeSb, NbFeSb, and NbCoSn), Sc (substituting Hf in HfCoSb), and Ti (for Ta in TaFeSb), with reductions ranging from 40% to 50% in the $10^{20}$–$10^{21}$ $cm^{-3}$ concentration range. In addition to the substitutional defects shown here, the thermal conductivity can be affected by other mechanisms, like the electron-phonon interaction, boundary scattering, and the formation of other defect structures, including Frenkel defects and intrinsic vacancies. We have argued that this is the case for (Ti,Hf)-doped NbFeSb and $Sn_{Sb}$-doped ZrCoSb. We have shown that a good match with conductivity measurements can be achieved if the scattering of phonons by Co Frenkel pairs is included, for a defect concentration slightly higher than the experimentally estimated one. Nevertheless, we obtain an almost perfect match if we rather assume Co vacancies and interstitials to be independent from each other, and we use the actual experimental concentrations. The independent vacancies and interstitials are energetically more favorable than Frenkel pairs, and are presumably the main reason for the low $\kappa_{ph}$ of tin-doped ZrCoSb.

Finally, we have fitted the thermal conductivity curves to an analytical two-parameter model that may be employed when evaluating $\kappa_{ph}$ at different temperatures and doping concentrations, and which could provide an easy way to study the impact of defects and phonon transport on the thermoelectric efficiency of HHs. The present findings show the general importance of the impurity-induced mass and force constant perturbations upon thermal transport properties, and showcase general trends regarding the impact of the bond perturbation upon scattering of phonons. These results may be useful in the design of doped half-Heusler compounds for thermoelectric applications.

## ACKNOWLEDGMENTS

This work was supported by project CODIS (Agence Nationale de la Recherche project ANR-17-CE08-0044-01 and Austrian Science Funds (FWF) Grant No. FWF-I-3576-N36).

[1] J. Ziman, *Electrons and Phonons: The Theory of Transport Phenomena in Solids*, International Series of Monographs on Physics (Oxford University Press, Oxford, 2001).
[2] G. Nolas, J. Sharp, and J. Goldsmid, *Thermoelectrics: Basic Principles and New Materials Developments*, Springer Series in Materials Science (Springer, Berlin, 2001).
[3] C. Fu, S. Bai, Y. Liu, Y. Tang, L. Chen, X. Zhao, and T. Zhu, Nat. Commun. **6**, 8144 (2015).
[4] H. Zhu, J. Mao, Y. Li, J. Sun, Y. Wang, Q. Zhu, G. Li, Q. Song, J. Zhou, Y. Fu *et al.*, Nat. Commun. **10**, 270 (2019).
[5] J. Zhou, H. Zhu, T.-H. Liu, Q. Song, R. He, J. Mao, Z. Liu, W. Ren, B. Liao, D. J. Singh *et al.*, Nat. Commun. **9**, 1721 (2018).
[6] A. S. Sharma, S. Das, S. A. Gazi, and S. Dhar, J. Appl. Phys. **126**, 155702 (2019).
[7] G. Naydenov, P. Hasnip, V. Lazarov, and M. Probert, J. Phys.: Mater. **2**, 035002 (2019).
[8] J. Yang, G. P. Meisner, and L. Chen, Appl. Phys. Lett. **85**, 1140 (2004).
[9] A. Petersen, S. Bhattacharya, T. M. Tritt, and S. J. Poon, J. Appl. Phys. **117**, 035706 (2015).
[10] S. Bhattacharya, M. J. Skove, M. Russell, T. M. Tritt, Y. Xia, V. Ponnambalam, S. J. Poon, and N. Thadhani, Phys. Rev. B **77**, 184203 (2008).
[11] S. Bhattacharya and G. K. H. Madsen, J. Mater. Chem. C **4**, 11261 (2016).
[12] M. Omini and A. Sparavigna, Phys. Rev. B **53**, 9064 (1996).
[13] D. A. Broido, M. Malorny, G. Birner, N. Mingo, and D. A. Stewart, Appl. Phys. Lett. **91**, 231922 (2007).
[14] W. Li, J. Carrete, N. A. Katcho, and N. Mingo, Comput. Phys. Commun. **185**, 1747 (2014).
[15] W. Li, N. Mingo, L. Lindsay, D. A. Broido, D. A. Stewart, and N. A. Katcho, Phys. Rev. B **85**, 195436 (2012).
[16] A. Ward, D. A. Broido, D. A. Stewart, and G. Deinzer, Phys. Rev. B **80**, 125203 (2009).
[17] S.-i. Tamura, Phys. Rev. B **27**, 858 (1983).
[18] S.-i. Tamura, Phys. Rev. B **30**, 849 (1984).
[19] N. H. Protik, J. Carrete, N. A. Katcho, N. Mingo, and D. Broido, Phys. Rev. B **94**, 045207 (2016).
[20] N. Mingo, K. Esfarjani, D. A. Broido, and D. A. Stewart, Phys. Rev. B **81**, 045408 (2010).
[21] E. N. Economou, *Green's Functions in Quantum Physics* (Springer, Heidelberg, 2006).
[22] A. Katre, J. Carrete, B. Dongre, G. K. H. Madsen, and N. Mingo, Phys. Rev. Lett. **119**, 075902 (2017).
[23] G. Kresse and J. Hafner, Phys. Rev. B **47**, 558 (1993).
[24] G. Kresse and J. Hafner, Phys. Rev. B **49**, 14251 (1994).
[25] G. Kresse and J. Furthmüller, Phys. Rev. B **54**, 11169 (1996).
[26] P. E. Blöchl, Phys. Rev. B **50**, 17953 (1994).
[27] G. Kresse and D. Joubert, Phys. Rev. B **59**, 1758 (1999).

[28] J. P. Perdew, K. Burke, and M. Ernzerhof, Phys. Rev. Lett. **77**, 3865 (1996).
[29] K. Burke, J. P. Perdew, and M. Ernzerhof, J. Chem. Phys. **109**, 3760 (1998).
[30] A. Togo and I. Tanaka, Scr. Mater. **108**, 1 (2015).
[31] A. Togo, F. Oba, and I. Tanaka, Phys. Rev. B **78**, 134106 (2008).
[32] W. Li, L. Lindsay, D. A. Broido, D. A. Stewart, and N. Mingo, Phys. Rev. B **86**, 174307 (2012).
[33] J. Carrete, B. Vermeersch, A. Katre, A. van Roekeghem, T. Wang, G. K. H. Madsen, and N. Mingo, Comput. Phys. Commun. **220**, 351 (2017).
[34] T. Graf, C. Felser, and S. S. P. Parkin, Prog. Solid State Chem. **39**, 1 (2011).
[35] J. Carrete, W. Li, N. Mingo, S. Wang, and S. Curtarolo, Phys. Rev. X **4**, 011019 (2014).
[36] X. Zhang, L. Yu, A. Zakutayev, and A. Zunger, Adv. Funct. Mater. **22**, 1425 (2012).
[37] See Supplemental Material at http://link.aps.org/supplemental/10.1103/PhysRevB.103.174112 for additional information and data regarding phononic and electronic densities of states, phonon-defect scattering rates, descriptors, and the linear chain model.
[38] F. Aliev, N. Brandt, V. Moshchalkov, V. Kozyrkov, R. Skolozdra, and A. Belogorokhov, Z. Phys. B: Condens. Matter **75**, 167 (1989).
[39] F. G. Aliev, V. V. Kozyrkov, V. V. Moshchalkov, R. V. Scolozdra, and K. Durczewski, Z. Phys. B: Condens. Matter **80**, 353 (1990).
[40] I. Galanakis and P. Mavropoulos, J. Phys.: Condens. Matter **19**, 315213 (2007).
[41] S. Chen and Z. Ren, Mater. Today **16**, 387 (2013).
[42] B. Dongre, J. Carrete, A. Katre, N. Mingo, and G. K. H. Madsen, J. Mater. Chem. C **6**, 4691 (2018).
[43] P. Klemens, Int. J. Thermophys. **22**, 265 (2001).
[44] R. He, T. Zhu, Y. Wang, U. Wolff, J.-C. Jaud, A. Sotnikov, P. Potapov, D. Wolf, P. Ying, M. Wood *et al.*, Energy Environ. Sci. **13**, 5165 (2020).
[45] B. Dongre, J. Carrete, S. Wen, J. Ma, W. Li, N. Mingo, and G. K. H. Madsen, J. Mater. Chem. A **8**, 1273 (2020).
[46] J. E. Douglas, C. S. Birkel, N. Verma, V. M. Miller, M.-S. Miao, G. D. Stucky, T. M. Pollock, and R. Seshadri, J. Appl. Phys. **115**, 043720 (2014).
[47] M. Wambach, R. Stern, S. Bhattacharya, P. Ziolkowski, E. Müller, G. K. H. Madsen, and A. Ludwig, Adv. Electron. Mater. **2**, 1500208 (2016).